Journal of Materials Chemistry C

Accepted Manuscript

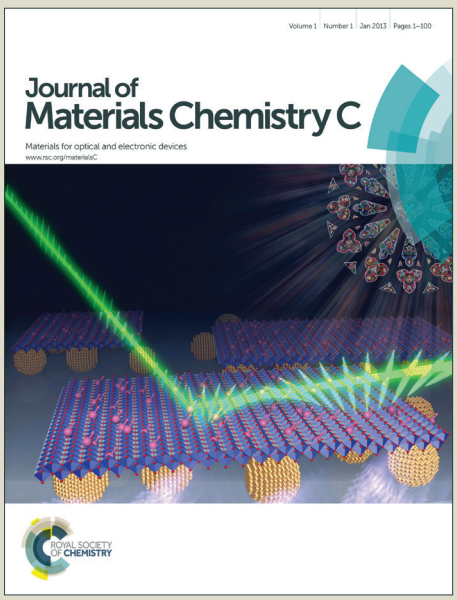

ROYAL SOCIETY OF CHEMISTRY

www.rsc.org/materialsC

Journal Name

ARTICLE

Kesterite Cu_2ZnSnS_4 thin film solar cells by a facile DMF-based solution coating process

Received 00th January 20xx,
Accepted 00th January 20xx

DOI: 10.1039/x0xx00000x

www.rsc.org/

Fangyang Liu,* [a, b] Shanshan Shen, [a] Fangzhou Zhou, [b] Ning Song, [b] Xiaoming Wen, [b] John A. Stride, [c] Kaiwen Sun, [b] ChangYan, [b] and Xiaojing Hao * [b]

Kesterite Cu_2ZnSnS_4 (CZTS) thin films were fabricated using a low-cost and environmentally friendly route from a dimethylformamide (DMF) solution of a metal–thiourea complex. Thermal gravimetric analysis (TGA) has been performed to reveal the thermal decomposition behavior of the CZTS precursors for drying and sulfurization process design. A facile solution method of *in-situ* introducing sodium dopant by adding NaOH into the precursor solution is presented. The sodium dopant improves the open circuit voltage (Voc) and fill factor (FF) and thereby enhances the power conversion efficiency from 4.47% to 5.68%. The enhanced performance is related to the increased grain size and elongated minority carrier lifetime. A large number of large voids observed in the bulk absorber and at the absorber/back contact interface are considered to be the main reason for the low short circuit current density (Jsc).

Introduction

Kesterite Cu_2ZnSnS_4 (CZTS) has recently attracted a great amount of interest as a potential absorber for next generation thin film solar cells, owing to its decent optical and electronic properties comparable to traditional Cu(In, Ga)Se_2 (CIGS) and CdTe materials, and constituents of earth abundant and nontoxic elements[1]. Similar to CIGS and CdTe, CZTS can be fabricated by both vacuum and solution based processes[2]. Typical vacuum based processes such as evaporation[3] and sputtering[4] may suffer from the high volatility of several elements or intermediate phases and the narrow compositional stability window of the CZTS phase, in addition to scaling issues and high intrinsic costs. In this regard, solution based processes are desirable and are actively being developed. Nanoparticle ink coating is a very viable solution based process, especially for Se-incorporated sulfoselenide ($Cu_2ZnSn(S, Se)_4$, CZTSSe) absorbers which show large grain microstructure through a post selenization under Se or H_2Se atmosphere and yield promising high power conversion efficiency of 7-10%[5-12]. Notably, a series of record-setting devices using CZTSSe absorbers with [S]/([S]+[Se]) of ~ 0.4 and band gap of ~1.13 eV have been developed by the IBM group using a hydrazine based hybrid solution-particle slurry and post selenization process[13, 14]. However, for pure sulfide CZTS, which is preferable from both an environmental compatibility perspective and the desire for optimal band gap of ~1.45 eV, nanoparticle ink coating seems to meet enormous challenges in fabricating absorbers with large grain and compact microstructure through post sulfurization due to the difficulties in long range diffusion and volume expansion without reactive incorporation of Se (larger atomic size than S)[15]. Besides, the nanoparticle coated approach potentially causes microscale non-uniformities in precursors[16]. In contrast with the aforementioned technologies, a pure solution approach can offer precursor homogeneity at a molecular scale and accordingly enable the precise stoichiometric control and excellent film consistency, which are necessary for low-cost and large-scale production. Moreover, it eliminates the need for long range diffusion, facilitating the formation of large grains. A number of solvents have been employed to fabricate kesterite materials. For sulfoselenide CZTSSe, some attractive power conversion efficiencies of 8.08% by hydrazine + hydrazinocarboxylic acid dissolution of Zn metal,[17] 6.52% by ethanol + 1-butylamine + 3-mercaptopropionic acid,[18] 5.14% [19] and 6.62% [20] by water, 6.16% by water + ethanol,[21] 6.83% for 2-methoxyethanol+ thioglycolic acid + monoethanolamine,[22] 8.32%[23] by dmethyl sulfoxide (DMSO), and 12.6% by hydrazine (record efficiency)[24] have been achieved by several groups. For sulfide CZTS, however, efficiency of CZTS devices from purely solution-based processes are much lower and only very few groups have reported CZTS devices reaching efficiencies higher than 3%: 3.02% by

a Dr. Fangyang Liu, Dr. Shanshan Shen
School of Metallurgy and Environment, Central South University, Changsha 410083 (China)
b Dr. Fangyang Liu,Dr. Fangzhou Zhou, Dr. Ning Song, Dr. Xiaoming Wen, Dr. Kaiwen Sun, Dr. Chang Yan, Dr. Xiaojing Hao
School of Photovoltaic and Renewable Energy Engineering, University of New South Wales, Sydney 2052 (Australia)
E-mail: fangyang.liu@unsw.edu.au; xj.hao@unsw.edu.au
c Prof. John A. Stride
School of Chemistry, University of New South Wales, Sydney 2052 (Australia)

† Footnotes relating to the title and/or authors should appear here.
Electronic Supplementary Information (ESI) available: [details of any supplementary information available should be included here]. See DOI: 10.1039/x0xx00000x

ethanol,[25] 5.29% by water + ethanol,[26] and 5.1%[27] and 5.7% [28] by 2-methoxyethanol. In order to obtain a high quality kesterite absorber and achieve greater efficiency, the selection of the solvent is extremely important. On the one hand, a good solvent should have a high solubility for metal sources (metal salts or oxides) and sulfur source (optionally, such as sulfur, thiourea or thioacetamide etc.), and low surface tension allowing the solution to spread easily with full coverage and free of streaks or voids, and on the other hand have suitable boiling point and vapor pressure, allowing the solvent to readily evaporate with minimal residue yet not leading to instability during the coating and drying processes and the deterioration of the film microstructure due to a too rapid volatilization process. DMF is a common solvent in many fields that meets the above necessary requirements. It has been used as solvent in spray pyrolysis for CZTS thin film fabrication (metal salts and sulfur powder as start materials needing stabilizer) [29], yielding efficiency of 0.51%[30] and solvothermal synthesised CZTS microparticles [31].

In this work, we report the fabrication of kesterite CZTS absorber via a solution coating route from DMF solution of a metal–thiourea complex. We first investigated the thermal decomposition behavior of CZTS precursor by thermal gravimetric analysis. Then a facile *in-situ* solution method introducing sodium dopant by adding NaOH to the precursor solution is presented. We also performed the material and device electrical studies based on several characterization techniques and concluded by briefly summarizing the results.

Experimental

The precursor solution was prepared by dissolving 11.98 g $Cu(CH_3COO)_2{\cdot}H_2O$ (0.06 mol, AR), 8.12 g $Zn(CH_3COO)_2{\cdot}2H_2O$ (0.037 mol, AR), 7.45 g $SnCl_2{\cdot}2H_2O$ (0.033 mol, AR) and 19.7 g $SC(NH_2)_2$ (0.26 mol, AR) into 100 mL dimethylformamide (DMF, AR) and stirring at 50 ºC for 1 hour to get a light yellow solution. The solution can be stable for 1 year. All chemical reagents were purchased from Sinopharm Chemical Reagent Co., ltd. The precursor solution was then spin-coated on molybdenum coated soda-lime glass (SLG) substrates at 4000 rpm for 20 s, followed by drying at 300 ºC for 8 min on a hot plate in air. This coating step was repeated 15 times to get a CZTS precursor film with a desired thickness. After that, the prepared precursor films were sulfurized at 580ºC in a sulfur/N_2 atmosphere for 40 mins with controlled sulfur partial pressure, to form the CZTS absorbers. The solar cell devices were completed by a chemical bath deposited 70 nm CdS buffer, followed by RF magnetron sputtered 50 nm intrinsic ZnO, and DC magnetron sputtered 400 nm ITO window layer sequentially. Finally Al was thermally evaporated on the ITO layer to form top contact fingers via a shadow mask. Each device had a total area of approximately 0.45 cm^2 defined by mechanical scribing.

The surface and cross-sectional morphology of the thin films were characterized by SEM (NOVA NanoSEM 230). The X-ray diffraction (XRD) patterns and Raman spectra were collected by using Rigaku-TTR III X and Jobin-Yvon LabRAM HR-800 (514 nm and 325 nm excitation wavelength), respectively. An energy dispersive spectrometer (EDS, EDAX-GENSIS60S in NOVA NanoSEM 230) was used to check the elemental composition and its distribution. Elements identification and related valence state analysis was also conducted by X-Ray Photoelectron Spectroscopy (XPS, ESCALAB220i). A FEI Tecnai G2 equipped with energy dispersive spectroscopy detector was used for the transmission electron microscopy (TEM) analyses. Current density-voltage (*J*-V) characterization for the solar cells were performed using Xe-based light source solar simulator (Newport, 91160 and KEITHLEY 2400) to provide simulated 1 sun AM 1.5G illumination which was calibrated with a standard Si reference cell, traceable to the National Renewable Energy Laboratory. The external quantum efficiency (EQE) was measured using chopped monochromator beam and lock-in amplifier, with calibration into the NIR by Si and Ge diodes measurements (QEX10 spectral response system from PV measurements, Inc). Time-resolved photoluminescence (TRPL) measurements were performed on the device using the time-correlated single photon counting (TCSPC) technique (Microtime200, Picoquant) at a wavelength near the band gap. The excitation is a 467 nm laser with tunable repetition.

Results and Discussion

The thermal decomposition behavior of CZTS precursor was studied by thermal gravimetric analysis (TGA) in N_2 atmosphere as shown in **Figure 1**. The weight loss starts from about 155ºC corresponding to the boiling point of DMF and the first weight loss regime before around 220ºC represents the loss of DMF solvent. The weight loss regime from 220 to 310 ºC corresponds to the thermal decomposition of metal-thiourea complexes. The thermal decomposition mechanism of the metal-thiourea complexes has been investigated in detail in previous reports[27, 32]. Metal sulfides, and few metal oxides which can be converted into sulfides by subsequent high temperature sulfurization, are often formed during the thermal decomposition process. The very slow weight loss in the regime from 310 ºC to 550 °C is due to the oxidation of the sulfides. Therefore, the drying temperature should be set suitably in order to decompose the metal–thiourea complexes completely

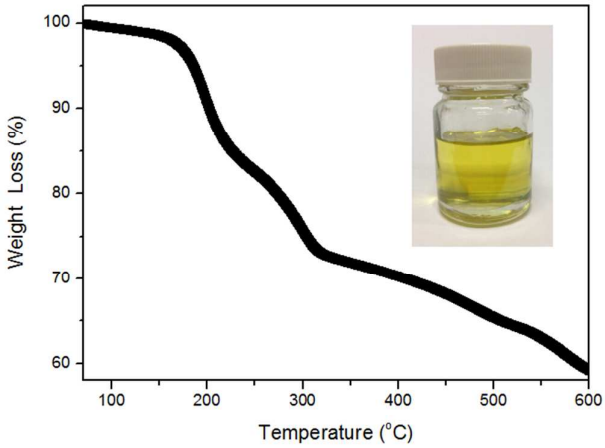

Figure 1. TGA curve of CZTS precursor from drying the solution at 100 °C for several hours to evaporate most solvent. The inset shows the CZTS precursor solution by solving metal salts and thiourea into DMF.

without excessive oxidation during the annealing in air. Although the thermal decomposition of the metal-thiourea complexes under an inert atmosphere contributes to the reduction of oxides, decomposition under an oxygen atmosphere is more favorable to decrease the content of carbon or nitrogen in the thin films by breaking and oxidizing the C-H or C-N bonds in the organic solvents[27]. Therefore, in this route, the drying process was performed at 300 ºC under air atmosphere.

Figure 2 shows the top-view and cross-sectional SEM images of the as-prepared CZTS precursor film by repeating the spin-coating and air drying procedure 15 times. The precursor exhibits a crack-free and three-dimensional porous morphology, which is beneficial to relieve the stress from volume contraction during air drying and expansion during sulfurization. The thickness is estimated to be about 1 µm. From EDS composition measurements, the metallic ratios of Cu/(Zn+Sn) and Zn/Sn in the precursor film are 0.86 and 1.13, respectively, remaining almost unchanged compared with those in the precursor solution. From the XRD pattern of the as-prepared precursor sample via drying in air at 300ºC (**Figure 1S**), three main diffraction peaks which match (112) (220) (312) reflections of kesterite CZTS phase are observed and the broad peak width indicates a relatively small grain size (~11 nm calculated using the Scherrer equation), confirming that kesterite CZTS nanocrystal precursors can be directly prepared by this simple molecular precursor-based solution route without the need of complex nanocrystal synthesis. Raman spectroscopy was employed to further investigate phase constitution of the as-prepared precursor, considering the low XRD signals from minor secondary phases (such as tin sulfide and copper sulfide) and the characteristic (110) peak of CZTS at poor crystallinity, and the overlap of the main peaks of CZTS, ZnS and Cu_2SnS_3. Raman spectrum, measured using 514 nm excitation wavelength in **Figure 2S (a),** shows an ambiguous peak at about 330 cm^{-1}, with a shoulder at about 338 cm^{-1} corresponding to the kesterite CZTS phase[33] and a peak at about 470 cm^{-1} which can be assigned to be $Cu_{2-x}S$ phases[34, 35]. The Raman peak at about 330 cm^{-1} may be attributed to be Cu_2SnS_3 (CTS) phase [34, 36] or a mixture of phases (CZTS and CTS)[37] considering the shift of the CZTS Raman peak to low wavenumbers with the decrease of Zn content[38]. The formation of kesterite CZTS phase from precursor solution at low temperature suggests a kinetically viable transformation that does not rely on the long-range motion of precursor constituents.[17] In addition, in order to determine the possible presence of ZnS phase, Raman spectrum was also recorded using a 325 nm excitation wavelength, which can enhance the detection sensibility of ZnS [39] and is show in **Figure 2S (b)**. The distinguishable, but very weak, peaks at 345 cm^{-1} and 697 cm^{-1} arising from the first-order and second-order ZnS bands [39] suggest very little ZnS phase present in the precursor. Besides, the existence of $Cu_{2-x}S$ phase from the peak at 475 cm^{-1} is observed again.

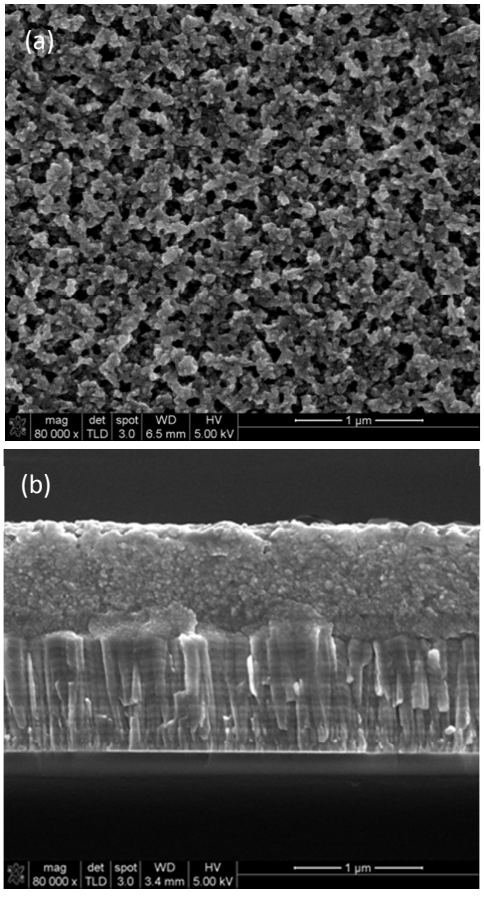

Figure 2. Top-view (a) and cross-sectional (b) SEM images of the as-prepared CZTS nanocrystal precursor film by repeating the spin-coating and air drying (300 ^oC in air) procedure 15 times.

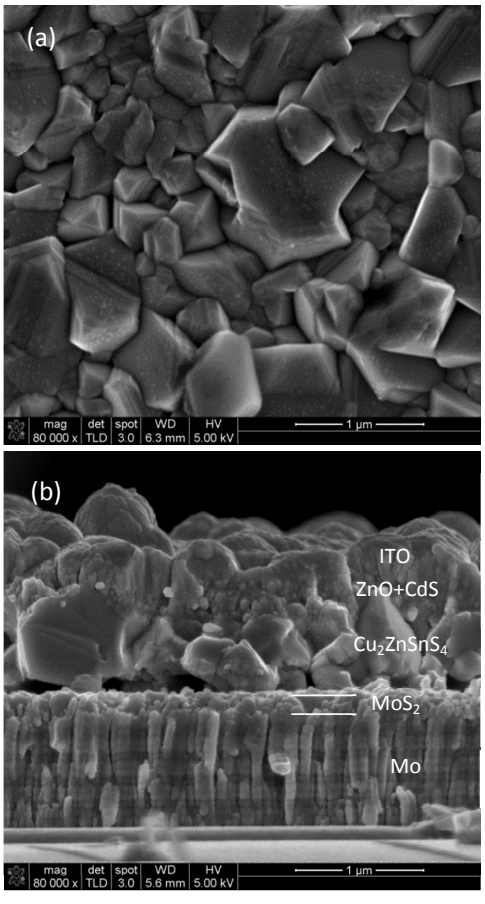

Figure 3. Top-view and cross-sectional SEM images of the CZTS absorber by sulfurizing the precursor at 580 ^oC in sulfur atmosphere

The final weight loss regime above 550 ºC in the TGA curve corresponds to the slow decomposition of the kesterite CZTS phase, forming the volatile species such as sulfur vapor and Sn(II) sulfide.[40] The addition of excess sulfur and optionally, tin sulfides, is suggested during sulfurization processes to inhibit the decomposition of the kesterite phase at high temperature and the presence of the detrimental impurity phases, and promote the grain growth. In our absorber preparation process, saturated sulfur vapor was provided during sulfurization, and so the sulfurization temperature can be as high as 560 ºC to 580 ºC. Too low sulfurization temperature will lead to poor crystallinity and small grain size (**Figure 3S (a)**), while too high sulfurization temperature will worsen the microstructure forming pinhole (**Figure 3S (b)**),and lead to excess thickness of high resistivity MoS_2 interface layer between CZTS and Mo back contact(**Figure 3S (c)**). In this work, the sulfurization temperature is chosen to be 580 ºC. **Figure 3a** shows a top-view SEM image of the typical CZTS absorber. The film shows dramatic morphology changes after sulfurization, exhibiting densely packed grains with a very uneven size, in the range of 0.2 - 1 µm. Most of the grains have a size smaller than 0.5 µm. From the cross sectional SEM image of the corresponding CZTS solar cell device, it is shown that the absorber is composed of a few large grains spanning the entre layer with thickness of near 1 µm but most of the grains do not extend from the back to the front of the film. The carbon-rich and (or) fine grain bottom layer frequently observed in absorbers synthesized by solution processes using other organic solvents[16,20,41] cannot be found here, whilst a lot of voids are visible at the bottom region of the absorber and the MoS_2 layer, with a thickness of about 200 nm is observable. For composition, the absorber has a Cu/(Zn+Sn) ratio of 0.90 and a Zn/Sn ratio of 1.15, which shows very little decrease in Sn content. This Cu-poor and Zn-rich composition is reported desirable for high-efficiency CZTS solar cells. **Figure 4a** shows the XRD pattern of the CZTS absorber film obtained by sulfurizing the as-prepared precursor. The XRD peaks sharpen considerably, indicating a large grain size, which is required for high performance CZTS solar cells, and show an excellent match to the kesterite phase with all of the minor reflections[41]. Raman spectroscopy was used again to investigate the phase purity of the CZTS absorber. From the Raman spectrum recorded using 514 nm excitation wavelength in **Figure 4b**, all distinctive peaks are in agreement with well-known vibrational characteristics of kesterite CTZTS phase[33, 42] without the observable secondary phases such as $Cu_{2-x}S$, SnS and Cu_2SnS_3. The Raman spectrum recorded using an excitation wavelength of 325 nm, as shown in the inset of **Figure 4b,** exhibits three peaks arising from the first-order, second-order and third-order ZnS bands, indicating the presence of ZnS phase, consistent with the Zn-rich composition. According to previous reports, a small amount of ZnS can help passivating the CZTS grain boundaries[43, 44] and obtaining high Voc,[27] although if too much would lead to current block and low short circuit current density (Jsc)[45, 46], having no significant negative effect on the efficiency of kesterite solar cells[47, 48]. The complementary studies based on XRD and Raman spectroscopy confirmed that the absorbers consists of a main phase of CZTS and a minor ZnS secondary phase after the sulfurization at 580 °C in sulfur atmosphere.

X-ray photoelectron spectroscopy (XPS) was performed to investigate the chemical states of the constituent elements and the

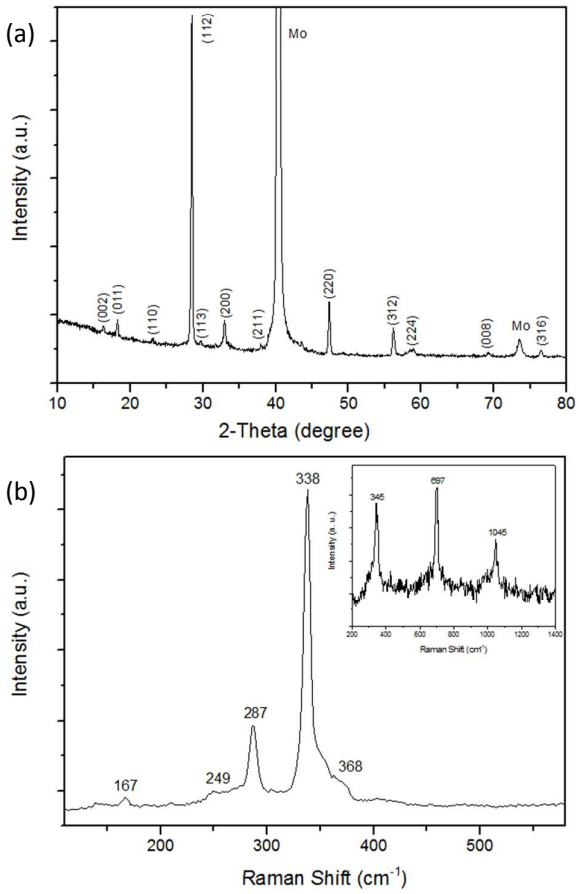

Figure 4. (a) XRD pattern of the CZTS absorber (b) Raman spectrum of the CZTS absorber measured with laser excitation wavelength of 514 nm. The inset shows the Raman spectrum measured with laser excitation wavelength of 325 nm.

concentration of impurities within the CZTS absorber after sulfurization. The XPS spectra of all four elements are shown in **Figure 4S**. The peak of Cu 2p is split into two separate features at 931.7 (2p3/2) and 951.5 eV (2p1/2), with a splitting of 19.8 eV, which is in good accordance with the value of Cu(I). The peaks of Zn 2p appear at binding energies of 1021.4 and 1044.5 eV, which can be assigned to Zn(II) with a peak splitting of 23.1 eV. The peaks of Sn 3d peaks located at 486.9 and 495.4 eV with a splitting value of 8.5 eV, correspond to Sn(IV). The sulfur 2p peaks in the spectra are located at 162.7 and 161.6 eV with a doublet separation of 1.1 eV, which is consistent with the 160-164 eV range of S in the sulphide phases. These XPS data, in agreement with the reported values in the literatures [37, 49, 50] demonstrate that Cu_2ZnSnS_4 is formed. Unlike vacuum-based methods, the organic solution-based processing of metal chalcogenides will inevitably lead to residual impurities, such as C, O, N and Cl, in CZTS thin films. **Figure 5** shows the changes in impurity elements for precursor and CZTS absorber. The atomic percentages of Cl, C, N and O are 4.34%, 5.35%, 2.25% and 15.47%, respectively for the precursor. For the absorber, the XPS signals from Cl and N disappear, indicating that the content of Cl and N is below the detection limit of XPS (< 0.1%). The atomic percentage of O also shows a significant decrease to 0.78%, revealing that the oxygen in precursor is almost removed during sulfurization. There is

still some residual carbon impurities with atomic percentage of 2.12% after sulfurization and the C 1s peak was observed to shift from a binding energy in the range of 285 - 287 eV to about 284 eV, indicating the change of the C-atoms bonding structure from C-O and C-N to C-C[51-53] after sulfurization. According to previous experience in kesterite[25, 27, 54] and chalcopyrite[55] photovoltaics, this concentration level of carbon residue is very low and acceptable for high-efficiency device fabrication although the tolerable concentrations has not yet been deeply investigated. Meanwhile, compared to several hundreds of nanometers thick carbon residual layers in films formed via solution processes using other solvent[18, 23, 47, 56], the facile removal of carbon in this process is believed to be an advantage of using DMF as the solvent. Considering that carbon impurities in absorbers have been considered to be detrimental to efficiency of the solar cells[57-59], further efforts on completing removal of carbon impurity are needed.

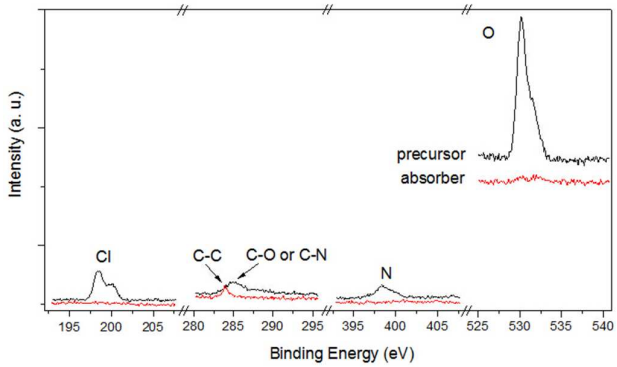

Figure 5. High-resolution XPS scan of impurities in CZTS precursor and absorber using the same set of parameters.

It has been reported that sodium is essential for absorber microstructure and electronic properties improvement, and thereby enhance the device performance[60-63]. Although sodium is usually provided by the SLG substrates via diffusion during high temperature sulfurization, the addition of extra sodium can further improve the performance of the device for both solution[18, 27, 64] and vacuum[65] based processes. Herein, an *in-situ* doping route was used: 0.003 g NaOH as sodium dopant source was added into the 100 ml precursor solution (3 mmol/L, so the Na doping amount is 1 mol.%) aiming to further promote the grain growth and improve the electronic properties of CZTS thin films. **Figure 6** shows the top-view SEM image of the Na-doped CZTS thin film and cross-sectional SEM images of corresponding CZTS solar cell device on a SLG substrate. It is observed from the top-view SEM image that the film consists of mainly large grains, with most of grain size larger than 1 µm, and some smaller grains between them. The average grain size is higher than that of the CZTS absorber without extra Na doping. Moreover, the addition of Na makes the film seem less angular and smoother, which is similar to the observation by Wangen Zhao et al. when adding 1% sodium diethyldithiocarbamate into ethanol solution[18]. From the cross-sectional SEM image, it is observed that more large grains extend through the entire depth of the film compared to CZTS absorber without extra Na doping. Therefore, the extra addition of Na has a beneficial effect on grain growth. Note that voids at the bottom region are still visible and the addition of extra Na does not significantly affect the MoS_2 thickness.

Figure 7a shows the photoluminescence (PL) spectra of the finished devices using DMF processed CZTS absorbers with and without Na

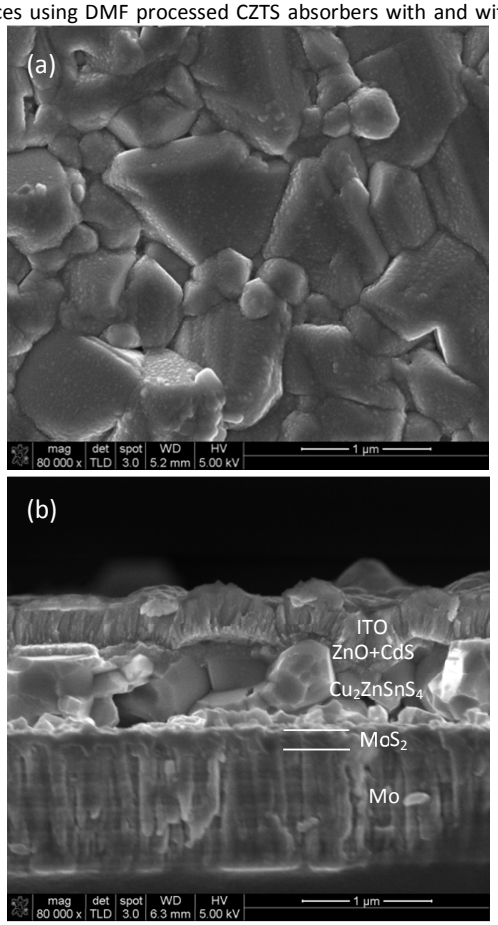

Figure 6. Top-view (a) and cross-sectional (b) SEM images of the CZTS absorber with extra Na doping by adding 3 mmol/L NaOH in precursor solution.

doping. Both PL spectra have the similar shape and consist of two bands at 1.30 and 1.39 eV, which originate from disordered and ordered pure kesterite CZTS[66] respectively and are lower than the reported band gap of CZTS (~1.45 eV). The photoluminescence bands in the range of 1.2eV - 1.4 eV below the band gap of CZTS have been reported widely for single crystals[67, 68], thin films[69-73], and monograin powders[74], pointing to the defect related recombination in CZTS thin films. The relatively weak transitions from band to band in the PL spectra indicate that defect-assisted recombination is the dominant process due to the large number of defects in the CZTS material. The PL intensity of CZTS device with extra Na doping is stronger than that of CZTS device without Na doping, suggesting that extra Na doping reduces/passivates defects in CZTS absorber and thus enhances the photoluminescence, which act as minor-carrier traps leading to recombination, and most likely origin from grain boundaries based on above SEM microstructure analysis.

The time-resolved photoluminescence (TRPL) was performed to check the minority carrier lifetime of the two devices, as shown in **Figure 7b**. We use bi-exponential fitting to analyse the curves as described by B. Ohnesorge et al. [75] The initial fast decay is ascribed to a radiative recombination process in the high-injection regime immediately after the laser pulse with the optically excited excess carrier concentration. The slow decay component is generally attributed to the minority carrier lifetime due to recombination.[76, 77] The minority carrier lifetime of 4.16±0.05 and 3.15±0.05 ns were extracted for CZTS devices with and without extra Na doping, respectively. The longer minority carrier lifetime for CZTS device with extra Na doping reveals slow recombination, consistent with previous reports[62, 65]. Note that the lifetime values in this work are comparable to those of pure sulfide CZTS devices reported by other groups[62, 71, 78] but lower than those of Se-incorporated CZTSSe devices[13, 79].

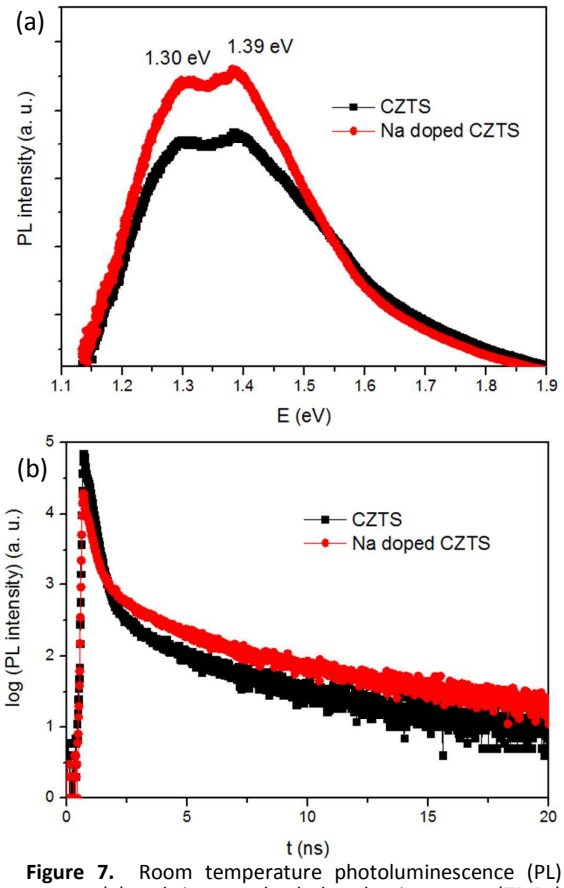

Figure 7. Room temperature photoluminescence (PL) spectra (a) and time-resolved photoluminescence (TR-PL) trace at the emission wavelength of 900 nm (b) of the finished devices with CZTS (black) and Na doped CZTS (red) absorbers.

CZTS and Na-doped CZTS devices exhibit the power conversion efficiency values in the range of 5-6% and 4-5%, respectively, as exhibited in **Figure 5S**. **Figure 8a** shows the current density-voltage (J-V) characteristics of the typical CZTS and Na-doped CZTS solar cells measured under dark and simulated AM1.5 illumination. A significant boost in PCE is observed from 4.77% to 5.68% for Na-doped CZTS solar cell. This enhancement is mainly due to the improvement in open circuit voltage (Voc) from 606 mV to 654 mV and fill factor (FF) from 55.2% to 58.9%, which closely relate to the lower carrier recombination and is in accord with the phenomena in previous reports[27, 62, 64, 65]. **Figure 8b** shows the external quantum efficiencies (EQE) of the two devices. The integrated short-circuit current densities extracted from the EQE data are 14.4 and 15.2 mA/cm^2 for CZTS and Na-doped CZTS devices, respectively, in good agreement with those obtained by *J*-V test under simulated sunlight. The slightly higher Jsc for Na-doped CZTS device is found from a higher response in the long wavelength region, meaning better carrier collection efficiency for Na-doped CZTS devices. Because sodium has been reported to cause narrower depletion width leading to lower Jsc[65] and carrier collection efficiency is most likely limited by carrier life time in CZTS based solar cells[41], the slight improvement in carrier collecting efficiency and Jsc may be attributed to the longer minority carrier lifetime for Na-doped CZTS device. The boost in performance for Na-doped CZTS device demonstrates the positive effect of Na spices in CZTS solar cells and effective sodium incorporation for current process.

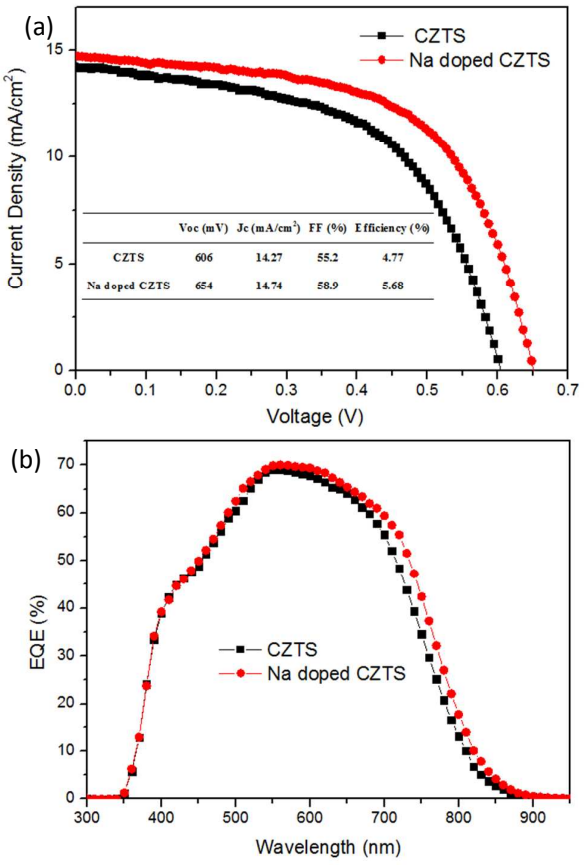

Figure 8. (a) Current density–voltage (J–V) characteristics and (b) external quantum efficiency (EQE) curves of the devices with CZTS (black) and Na doped CZTS (red) absorbers.

To gain insight into the properties of the CZTS solar cell in detail, the cross-sectional morphologies and compositional depth profile of the device were investigated using transmission electron microscopy (TEM) and EDS, respectively, as shown in **Figure 9**. The TEM image and the EDS line scans show that there are some big grains as large as the film thickness, with homogeneous elemental distribution and the absence of a fine grain bottom layer, or secondary phase grain such as ZnS which is frequently observed at the absorber/back contact interface[25, 71, 80, 81]. However, many large voids in the bulk absorber and at the bottom region of the absorber are clearly observable. Voids reduce absorption efficiency at long wavelength when in the bulk absorber and block the carrier transportation when at the bottom region of the absorber, which both are detrimental to device performance, especially Jsc. This may be the main reason for low Jcs in our devices, which is the most serious shortage compared to those CZTS devices yielding efficiencies higher than 7% with Jsc at the level of ~ 20 mA/cm^2 [71, 81-83]. Hence, one of the main factors for achieving higher efficiency in the present device is likely to diminish/eliminate the voids in the bulk absorber and at the absorber/back contact interface. In addition, the MoS_2 layer with a thickness of about 200 nm is observed between CZTS absorber and Mo. MoS_2 layer with low electrical conductivity facilitates the electrical quasi-ohmic contact and improves the adhesion of CZTS to the Mo back contact, but leads to high series resistance and accordingly deteriorates the device efficiency by decrease Jsc and FF if not thin enough,[84, 85] similar to the case of Cu(In, Ga)Se_2 solar cells.[86] Therefore, the further optimization to minimize MoS_2 thickness for Jsc improvement is also needed and is under investigation.

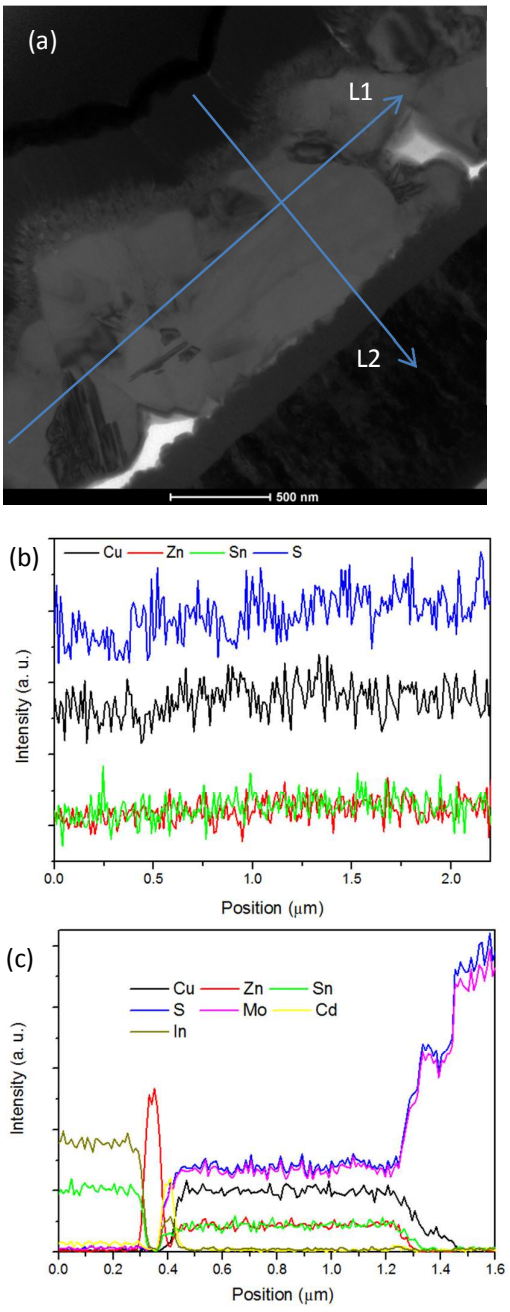

Figure 9. (a) Cross-sectional TEM image (Bright field) of the CZTS device milled by a focused ion beam technique. (b) and (c) the corresponding EDS line scans taken along the directions of the arrows L1 and L2 in the TEM image in (a), respectively. The diffusion of indium from ITO into CdS buffer layer is also observed. Due to overlap of S-Ka and Mo-La peaks in EDS, the S distribution actually is the combination of Mo and S.

Conclusions

In summary, we report the fabrication of CZTS thin films by a low-cost, scalable, and environmentally friendly solution-based route. In this route, melt salts and thiourea were dissolved in DMF solution, forming a homogeneous CZTS precursor solution from which CZTS nanocrystalline thin films were deposited. The drying and sulfurization were carried out at 300°C in air atmosphere and 580°C in saturated sulfur atmosphere, respectively. Through this solution based route, kesterite CZTS thin films with densely packed grains and no evidence of carbon-rich and (or) fine grain bottom layer, were obtained. Addition of extra Na dopant in the absorber from a facile solution incorporation simply by adding NaOH into the precursor solution has been achieved. This additional Na doping was found to improve the open circuit voltage (Voc) and fill factor (FF) and thereby boost the power conversion efficiency from 4.47% to 5.66%. The enhanced performance is related to the increased grain size and elongated minority carrier lifetime, leading to less recombination. A lot of large voids observed in the bulk absorber and at the absorber/back contact interface are considered to be the main reason for low short cicuit current density (Jsc). Future study will be focused on addressing the voids and MoS_2 issues to improve Jsc. More importantly, this solution route and doping way could be extended to fabricate other chalcogenide semiconductor thin film photovoltaics or flexible photovoltaics.

Acknowledgements

This Program has been supported by Hunan Provincial Natural Science Foundation of China (2015JJ2175) and the Australian Government through the Australian Renewable Energy Agency (ARENA) and Australian Research Council (ARC). Responsibility

for the views, information or advice expressed herein is not accepted by the Australian Government. The authors acknowledge the facilities, and the scientific and technical assistance of the Australian Microscopy & Microanalysis Research Facility at the Electron Microscope Unit, University of New South Wales (UNSW).

1. D. Aldakov, A. Lefrancois and P. Reiss, *Journal of Materials Chemistry C*, 2013, **1**, 3756-3776.
2. M. P. Suryawanshi, G. L. Agawane, S. M. Bhosale, S. W. Shin, P. S. Patil, J. H. Kim and A. V. Moholkar, *Mater. Technol.*, 2013, **28**, 98-109.
3. B. A. Schubert, B. Marsen, S. Cinque, T. Unold, R. Klenk, S. Schorr and H. W. Schock, *Prog Photovoltaics*, 2011, **19**, 93-96.
4. C. Platzer-Bjorkman, J. Scragg, H. Flammersberger, T. Kubart and M. Edoff, *Solar Energy Materials and Solar Cells*, 2012, **98**, 110-117.
5. W. Wu, Y. Cao, J. V. Caspar, Q. Guo, L. K. Johnson, I. Malajovich, H. D. Rosenfeld and K. R. Choudhury, *Journal of Materials Chemistry C*, 2014, **2**, 3777-3781.
6. Q. Guo, G. M. Ford, W. C. Yang, B. C. Walker, E. A. Stach, H. W. Hillhouse and R. Agrawal, *J Am Chem Soc*, 2010, **132**, 17384-17386.
7. W.-C. Hsu, H. Zhou, S. Luo, T.-B. Song, Y.-T. Hsieh, H.-S. Duan, S. Ye, W. Yang, C.-J. Hsu, C. Jiang, B. Bob and Y. Yang, *Acs Nano*, 2014, 164-9172.
8. J. van Embden, A. S. Chesman, E. Della Gaspera, N. W. Duffy, S. E. Watkins and J. J. Jasieniak, *J Am Chem Soc*, 2014, **136**, 5237-5240.
9. W.-C. Yang, C. K. Miskin, C. J. Hages, E. C. Hanley, C. Handwerker, E. A. Stach and R. Agrawal, *Chem Mater*, 2014, **26**, 3530-3534.
10. Q. Guo, J. V. Caspar, K. E. Roelofs, S. Subramoney and H. D. Rosenfeld, *Chem Mater*, 2014, **26**, 5664-5674.
11. Y. Cao, M. S. Denny, J. V. Caspar, W. E. Farneth, Q. Guo, A. S. Ionkin, L. K. Johnson, M. Lu, I. Malajovich, D. Radu, H. D. Rosenfeld, K. R. Choudhury and W. Wu, *J Am Chem Soc*, 2012, **134**, 15644-15647.
12. G. Larramona, S. Bourdais, A. Jacob, C. Choné, T. Muto, Y. Cuccaro, B. Delatouche, C. Moisan, D. Péré and G. Dennler, *The Journal of Physical Chemistry Letters*, 2014, 3763-3767.
13. T. K. Todorov, J. Tang, S. Bag, O. Gunawan, T. Gokmen, Y. Zhu and D. B. Mitzi, *Adv Energy Mater*, 2013, **3**, 34-38.
14. J. Kim, H. Hiroi, T. K. Todorov, O. Gunawan, M. Kuwahara, T. Gokmen, D. Nair, M. Hopstaken, B. Shin, Y. S. Lee, W. Wang, H. Sugimoto and D. B. Mitzi, *Adv Mater*, 2014, **26**, 7427-7431.
15. S. C. Riha, B. A. Parkinson and A. L. Prieto, *J Am Chem Soc*, 2011, **133**, 15272-15275.
16. T. Todorov, H. Sugimoto, O. Gunawan, T. Gokmen and D. B. Mitzi, *Ieee J Photovolt*, 2014, **4**, 483-485.
17. W. Yang, H.-S. Duan, B. Bob, H. Zhou, B. Lei, C.-H. Chung, S.-H. Li, W. W. Hou and Y. Yang, *Adv Mater*, 2012, **24**, 6323-6329.
18. W. Zhao, G. Wang, Q. Tian, Y. Yang, L. Huang and D. Pan, *Acs Appl Mater Inter*, 2014, **6**, 12650-12655.
19. J. Zhong, Z. Xia, C. Zhang, B. Li, X. Liu, Y.-B. Cheng and J. Tang, *Chem Mater*, 2014, **26**, 3573-3578.
20. Q. Tian, L. Huang, W. Zhao, Y. Yang, G. Wang and D. Pan, *Green Chemistry*, 2015, **17**, 1269-1275.
21. M. L. Jiang, F. Lan, X. Z. Yan and G. Y. Li, *Phys Status Solidi-R*, 2014, **8**, 223-227.
22. Q. Tian, G. Wang, W. Zhao, Y. Chen, Y. Yang, L. Huang and D. Pan, *Chem Mater*, 2014, **26**, 3098-3103.
23. H. Xin, J. K. Katahara, I. L. Braly and H. W. Hillhouse, *Adv Energy Mater*, 2014, **4**, 1301823.
24. W. Wang, M. T. Winkler, O. Gunawan, T. Gokmen, T. K. Todorov, Y. Zhu and D. B. Mitzi, *Adv Energy Mater*, 2014, **4**, 1301465.
25. J. W. Cho, A. Ismail, S. J. Park, W. Kim, S. Yoon and B. K. Min, *Acs Appl Mater Inter*, 2013, **5**, 4162-4165.
26. S.-N. Park, S.-J. Sung, D.-H. Son, D.-H. Kim, M. Gansukh, H. Cheong and J.-K. Kang, *RSC Advances*, 2014, **4**, 9118-9125.
27. Z. Su, K. Sun, Z. Han, H. Cui, F. Liu, Y. Lai, J. Li, X. Hao, Y. Liu and M. A. Green, *Journal of Materials Chemistry A*, 2014, **2**, 500-509.
28. K. Zhang, Z. Su, L. Zhao, C. Yan, F. Liu, H. Cui, X. Hao and Y. Liu, *Appl Phys Lett*, 2014, **104**, 141101.
29. T. Kunihiko, K. Minoru, G. Koichi, N. Yuya and U. Hisao, *Jpn J Appl Phys*, 2012, **51**, 10NC26.
30. K. Masato, T. Kunihiko, M. Katsuhiko and U. Hisao, *Jpn J Appl Phys*, 2012, **51**, 10NC33.
31. R. Saravana Kumar, C.-H. Hong and M.-D. Kim, *Advanced Powder Technology*, 2014, **25**, 1554-1559.
32. T. K. Chaudhuri and D. Tiwari, *Solar Energy Materials and Solar Cells*, 2012, **101**, 46-50.
33. M. Altosaar, J. Raudoja, K. Timmo, M. Danilson, M. Grossberg, J. Krustok and E. Mellikov, *Phys Status Solidi A*, 2008, **205**, 167-170.
34. O. Vigil-Galán, M. Espíndola-Rodríguez, M. Courel, X. Fontané, D. Sylla, V. Izquierdo-Roca, A. Fairbrother, E. Saucedo and A. Pérez-Rodríguez, *Solar Energy Materials and Solar Cells*, 2013, **117**, 246-250.
35. P. A. Fernandes, P. M. P. Salome and A. F. da Cunha, *Thin Solid Films*, 2009, **517**, 2519-2523.
36. U. Chalapathi, Y. Jayasree, S. Uthanna and V. Sundara Raja, *physica status solidi (a)*, 2013, **210**, 2384-2390.
37. J. M. R. Tan, Y. H. Lee, S. Pedireddy, T. Baikie, X. Y. Ling and L. H. Wong, *J Am Chem Soc*, 2014, **136**, 6684-6692.
38. Y. Chen, C.-H. Chuang, K.-C. Lin, S. Shen, C. McCleese, L. Guo and C. Burda, *The Journal of Physical Chemistry C*, 2014, **118**, 11954-11963.
39. X. Fontane, L. Calvo-Barrio, V. Izquierdo-Roca, E. Saucedo, A. Perez-Rodriguez, J. R. Morante, D. M. Berg, P. J. Dale and S. Siebentritt, *Appl Phys Lett*, 2011, **98**.
40. J. J. Scragg, T. Ericson, T. Kubart, M. Edoff and C. Platzer-Bjorkman, *Chem Mater*, 2011, **23**, 4625-4633.
41. D. B. Mitzi, O. Gunawan, T. K. Todorov, K. Wang and S. Guha, *Solar Energy Materials and Solar Cells*, 2011, **95**, 1421-1436.
42. T. Gurel, C. Sevik and T. Cagin, *Phys Rev B*, 2011, **84**.

43. B. G. Mendis, M. C. J. Goodman, J. D. Major, A. A. Taylor, K. Durose and D. P. Halliday, *J Appl Phys*, 2012, **112**, 124508-124510.
44. W. Bao and M. Ichimura, *Int J Photoenergy*, 2015, **2015**, 6.
45. J. Timo Wätjen, J. Engman, M. Edoff and C. Platzer-Björkman, *Appl Phys Lett*, 2012, **100**, 173510.
46. D. Colombara, E. V. C. Robert, A. Crossay, A. Taylor, M. Guennou, M. Arasimowicz, J. C. B. Malaquias, R. Djemour and P. J. Dale, *Solar Energy Materials and Solar Cells*, 2014, **123**, 220-227.
47. Y. Yang, G. Wang, W. Zhao, Q. Tian, L. Huang and D. Pan, *Acs Appl Mater Inter*, 2014, **7**, 460-464.
48. W.-C. Hsu, I. Repins, C. Beall, C. DeHart, G. Teeter, B. To, Y. Yang and R. Noufi, *Solar Energy Materials and Solar Cells*, 2013, **113**, 160-164.
49. M. D. Regulacio, C. Ye, S. H. Lim, M. Bosman, E. Y. Ye, S. Y. Chen, Q. H. Xu and M. Y. Han, *Chem-Eur J*, 2012, **18**, 3127-3131.
50. P. Kush, S. K. Ujjain, N. C. Mehra, P. Jha, R. K. Sharma and S. Deka, *Chemphyschem*, 2013, **14**, 2793-2799.
51. Y. Li, Y. Zhao, H. Cheng, Y. Hu, G. Shi, L. Dai and L. Qu, *J Am Chem Soc*, 2011, **134**, 15-18.
52. Z. Yang, M. Xu, Y. Liu, F. He, F. Gao, Y. Su, H. Wei and Y. Zhang, *Nanoscale*, 2014, **6**, 1890-1895.
53. Q. Liang, W. Ma, Y. Shi, Z. Li and X. Yang, *Carbon*, 2013, **60**, 421-428.
54. T. Schnabel, M. Löw and E. Ahlswede, *Solar Energy Materials and Solar Cells*, 2013, **117**, 324-328.
55. S. Ahn, T. H. Son, A. Cho, J. Gwak, J. H. Yun, K. Shin, S. K. Ahn, S. H. Park and K. Yoon, *Chemsuschem*, 2012, **5**, 1773-1777.
56. H. Guo, Y. Cui, Q. Tian, S. Gao, G. Wang and D. Pan, *Cryst Growth Des*, 2015, **15**, 771-777.
57. H. Azimi, Y. Hou and C. J. Brabec, *Energ Environ Sci*, 2014, **7**, 1829-1849.
58. H. Zhou, W.-C. Hsu, H.-S. Duan, B. Bob, W. Yang, T.-B. Song, C.-J. Hsu and Y. Yang, *Energ Environ Sci*, 2013, **6**, 2822-2838.
59. T. Todorov and D. B. Mitzi, *Eur J Inorg Chem*, 2010, 17-28.
60. M. Johnson, S. V. Baryshev, E. Thimsen, M. Manno, X. Zhang, I. V. Veryovkin, C. Leighton and E. S. Aydil, *Energ Environ Sci*, 2014, **7**, 1931-1938.
61. T. Prabhakar and N. Jampana, *Solar Energy Materials and Solar Cells*, 2011, **95**, 1001-1004.
62. H. Zhou, T.-B. Song, W.-C. Hsu, S. Luo, S. Ye, H.-S. Duan, C.-J. Hsu, W. Yang and Y. Yang, *J Am Chem Soc*, 2013, **135**, 15998-16001.
63. T. Gershon, B. Shin, N. Bojarczuk, M. Hopstaken, D. B. Mitzi and S. Guha, *Adv Energy Mater*, 2015, **5**, 1400849.
64. C. M. Sutter-Fella, J. A. Stückelberger, H. Hagendorfer, F. La Mattina, L. Kranz, S. Nishiwaki, A. R. Uhl, Y. E. Romanyuk and A. N. Tiwari, *Chem Mater*, 2014, **26**, 1420-1425.
65. J. V. Li, D. Kuciauskas, M. R. Young and I. L. Repins, *Appl Phys Lett*, 2013, **102**, 163905.
66. M. Grossberg, J. Krustok, J. Raudoja and T. Raadik, *Appl Phys Lett*, 2012, **101**, 102102.
67. S. Levcenko, V. E. Tezlevan, E. Arushanov, S. Schorr and T. Unold, *Phys Rev B*, 2012, **86**.
68. K. Tanaka, Y. Miyamoto, H. Uchiki, K. Nakazawa and H. Araki, *Phys Status Solidi A*, 2006, **203**, 2891-2896.
69. M. Yusuke, T. Kunihiko, O. Masatoshi, M. Noriko and U. Hisao, *Jpn J Appl Phys*, 2008, **47**, 596.
70. X. Lin, J. Kavalakkatt, K. Kornhuber, S. Levcenko, M. C. Lux-Steiner and A. Ennaoui, *Thin Solid Films*, 2013, **535**, 10-13.
71. B. Shin, O. Gunawan, Y. Zhu, N. A. Bojarczuk, S. J. Chey and S. Guha, *Progress in Photovoltaics: Research and Applications*, 2013, **21**, 72-76.
72. J. P. Leitao, N. M. Santos, P. A. Fernandes, P. M. P. Salome, A. F. da Cunha, J. C. Gonzalez, G. M. Ribeiro and F. M. Matinaga, *Phys Rev B*, 2011, **84**.
73. M. J. Romero, H. Du, G. Teeter, Y. F. Yan and M. M. Al-Jassim, *Phys Rev B*, 2011, **84**.
74. M. Grossberg, J. Krustok, J. Raudoja, K. Timmo, M. Altosaar and T. Raadik, *Thin Solid Films*, 2011, **519**, 7403-7406.
75. B. Ohnesorge, R. Weigand, G. Bacher, A. Forchel, W. Riedl and F. H. Karg, *Appl Phys Lett*, 1998, **73**, 1224-1226.
76. O. Gunawan, T. K. Todorov and D. B. Mitzi, *Appl Phys Lett*, 2010, **97**.
77. I. Repins, C. Beall, N. Vora, C. DeHart, D. Kuciauskas, P. Dippo, B. To, J. Mann, W.-C. Hsu, A. Goodrich and R. Noufi, *Solar Energy Materials and Solar Cells*, 2012, **101**, 154-159.
78. T. Gershon, B. Shin, N. Bojarczuk, T. Gokmen, S. Lu and S. Guha, *J Appl Phys*, 2013, **114**, 154905-154905-154905.
79. F. Liu, F. Zeng, N. Song, L. Jiang, Z. Han, Z. Su, C. Yan, X. Wen, X. Hao and Y. Liu, *Acs Appl Mater Inter*, 2015, **7**, 14376-14383.
80. J. T. Wätjen, J. J. Scragg, T. Ericson, M. Edoff and C. Platzer-Björkman, *Thin Solid Films*, 2013, **535**, 31-34.
81. F. Jiang, S. Ikeda, T. Harada and M. Matsumura, *Adv Energy Mater*, 2013, **4**, 1301381.
82. S. Ahmed, K. B. Reuter, O. Gunawan, L. Guo, L. T. Romankiw and H. Deligianni, *Adv Energy Mater*, 2012, **2**, 253-259.
83. J. J. Scragg, T. Kubart, J. T. Wätjen, T. Ericson, M. K. Linnarsson and C. Platzer-Björkman, *Chem Mater*, 2013, **25**, 3162-3171.
84. B. Shin, N. A. Bojarczuk and S. Guha, *Appl Phys Lett*, 2013, **102**, 091907-091904.
85. C. Puvaneswaran, H. Mohammad Istiaque, H. Jamilah, A. Mohammad, S. Kamaruzzaman and A. Nowshad, *Jpn J Appl Phys*, 2012, **51**, 10NC32.
86. X. Zhu, Z. Zhou, Y. Wang, L. Zhang, A. Li and F. Huang, *Solar Energy Materials and Solar Cells*, 2012, **101**, 57-61.

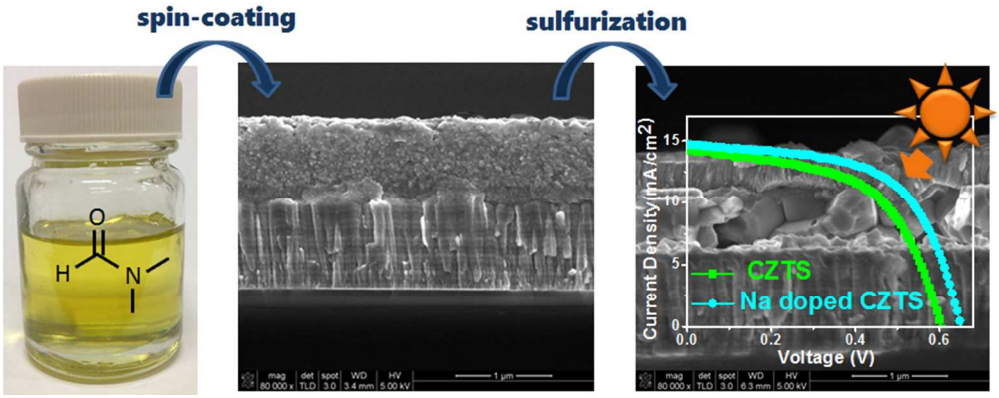

Schematic representation of the CZTS absorber and device in this study
242x94mm (96 x 96 DPI)